

# Hierarchies of entanglement potentials reveal intrinsic quantum state nonclassicality

Josef Kadlec,<sup>1</sup> Karol Bartkiewicz,<sup>2</sup> Antonín Černoš,<sup>3</sup> Karel Lemr,<sup>1</sup> and Adam Miranowicz<sup>2</sup>

<sup>1</sup>*Palacký University in Olomouc, Faculty of Science,  
Joint Laboratory of Optics of Palacký University and Institute of Physics AS CR,  
17. listopadu 12, 771 46 Olomouc, Czech Republic*

<sup>2</sup>*Institute of Spintronics and Quantum Information, Faculty of Physics,  
Adam Mickiewicz University, 61-614 Poznań, Poland*

<sup>3</sup>*Institute of Physics of the Academy of Sciences of the Czech Republic,  
Joint Laboratory of Optics of Palacký University and Institute of Physics AS CR,  
17. listopadu 50a, 772 07 Olomouc, Czech Republic*

(Dated: January 30, 2024)

Entanglement potentials are a promising method for the characterization of quantum state nonclassicality. Although they possess several interesting benefits, they critically rely on a well-tailored interaction between the tested state and a suitable classical state. We analyze the effect of imperfections in the interaction that are in real experiments to some extent always unavoidable. Furthermore, we study hierarchies of several entanglement potentials allowing us to detect these imperfections and, thus, preventing from misjudging the true intrinsic nonclassicality of the investigated states. The proposed idea is demonstrated in a proof-of-principle experiment on the platform of linear optics.

## I. INTRODUCTION

Nonclassical states of light play a key role in various quantum technologies, ranging from quantum communications and information processing to quantum metrology. Their properties facilitate inherently secure cryptography [1–3], supremacy of quantum computing [4] or imaging and sensing with resolutions above classical limits [5, 6]. Effective and experimentally suitable approach for nonclassicality description is, thus, an indispensable ingredient enabling these technologies.

A quantum-optical state is considered as nonclassical if its Glauber-Sudarshan  $P$  function is not positive semidefinite [7]. Based on this definition various measures of single-mode nonclassicality have been proposed and studied, such as, nonclassical distance [8], defined as a distance to a closest classical state, which is difficult to calculate even numerically, and nonclassical depth [9, 10] defined as the minimum amount of Gaussian noise required to obtain a classical state. This criteria is suitable for Gaussian states, but for any other nonclassical states, its value is equal to one. Other measures, not based upon the  $P$  function, include the entanglement potentials [11]. For a comparative study of these nonclassicality measures see reference [12]. Moreover, non-universal criteria (often referred to as nonclassicality witnesses) are often applied in quantifying single- or multi-mode nonclassicality. These include nonclassical volume [13], Wigner distinguishability [14], or the potentials for quantum steering and Bell nonlocality [15], among dozens of other criteria (see, e.g., [16] and references therein). Here we apply the entanglement potentials, which have a number of advantages compared to other methods: (i) some of the potentials can be easily calculated (as is shown in the later sections) contrary to, e.g., the nonclassical distance, (ii) they can distinguish the nonclassicality degree of wider variety of classes of states, compared to the nonclassical depth, (iii) they are measurable, as we have recently

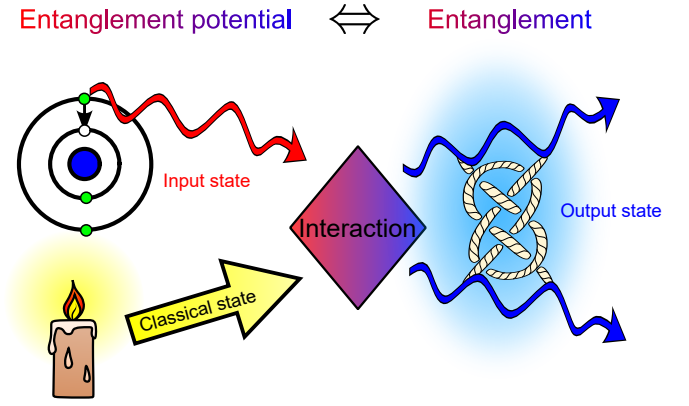


FIG. 1. Conceptual scheme of the entanglement potentials. A tested state interacts with a purely classical state. Entanglement detected in the output two-mode state reveals nonclassicality of the tested state and corresponds to its entanglement potential.

demonstrated experimentally [17], and (iv) they are universal [11], as required for good nonclassicality measures, and contrary to nonclassicality witnesses.

Considering the above cited, entanglement potentials prove to be a very convenient and experimentally feasible tool for describing and quantifying nonclassicality. Its concept is build upon the ability of a nonclassical state to produce entanglement by interacting with purely classical states, usually the vacuum (see Fig. 1). An example of this effect is the single-photon state that transforms into the Bell state after interacting with the vacuum on a balanced beam splitter.

A practical benefit of entanglement potentials is that they exploit the well developed formalism for quantifica-

tion of bipartite entanglement to describe single-mode nonclassicality. Moreover, any entanglement measure might be used to define the corresponding potential, thus, allowing us to gain a deeper understanding of nonclassicality, by studying mutual relations between various potentials for entanglement. In this work, we focus on the potentials for Wootters concurrence [18], negativity [19], and the relative entropy of entanglement (REE) [20].

The measured value of a given entanglement potential is affected by both the genuine properties of a tested state as well as the imperfections in its interaction with the chosen classical state. In this paper, we show that by analysing mutual relations between several potentials for standard entanglement measures, one can distinguish between these two effects. This capability makes the entanglement potentials a considerably more reliable tool for experimental nonclassicality quantification.

We support our theoretical predictions [21] by a proof-of-principle experiment on the platform of linear optics. In this experiment, we first generate the vacuum and one-photon superposition (VOPS) state that then interacts with the vacuum on a beam splitter. To avoid the need for experimentally demanding vacuum detection while reconstructing the output state, we encode the single-photon state into a horizontally polarized photon and for the vacuum we use vertically polarized photons as placeholders. We utilise the fact, that a vertically polarized photon state has a vacuum component in its horizontal mode, i.e.  $|0\rangle_H |1\rangle_V$ , where the numbers denote Fock states in the horizontal and vertical modes, respectively. For a more detailed description of the experimental implementation, see the Sec. III.

## II. ENTANGLEMENT POTENTIALS

We calculate entanglement potentials in VOPS states, which can be described by a density matrix

$$\sigma(p, y) = \begin{pmatrix} 1-p & y \\ y^* & p \end{pmatrix} \quad (1)$$

expressed in the basis of the vacuum,  $|0\rangle$ , and Fock single photon state  $|1\rangle$ , with  $p$  being the single-photon probability and  $y$  a coherence term. Alternatively, one can write  $y = e^{i\phi} D y_{\max}$ , where  $y_{\max} = \sqrt{(1-p)p}$  is the maximal possible absolute value of the coherence term,  $D \in [0, 1]$  is a dephasing factor, and  $\phi \in [0, 2\pi)$  is an arbitrary phase. The dephasing factor can be interpreted by assuming a pure state affected by a dephasing channel, with the phase-flip probability of  $f$ , then  $D = |1 - 2f|$ .

Upon interaction, the VOPS state on one port of a beam splitter (BS) and the classical vacuum state on the other port produce the output density matrix [15]

$$\rho_{wr}(p, y) = \begin{pmatrix} 1-p & -wry & wty & 0 \\ -wry^* & pr^2 & -pw^2rt & 0 \\ wty^* & -pw^2rt & pt^2 & 0 \\ 0 & 0 & 0 & 0 \end{pmatrix}, \quad (2)$$

in the basis  $\{|00\rangle, |01\rangle, |10\rangle, |11\rangle\}$ , where  $r$  and  $t$  are the reflection and transmission coefficients respectively. Due to the fact, that the phase of  $r$  and  $t$  does not affect any reasonable entanglement measure, we assume them both to be real non-negative. The interaction parameter  $w \in [0, 1]$ , with  $w = 1$  corresponding to a perfectly coherent interaction, influences the output state coherence.

The matrix in Eq. (2) can be used to calculate any entanglement measure. In this paper, we use negativity, concurrence, and the REE to quantify the output state entanglement. Note, that to acquire the true potential of the input state one needs to have a balanced ( $r = t = 1/\sqrt{2}$ ) non-decohering ( $w = 1$ ) beam splitter, otherwise the value of the observed potential is diminished due to imperfect interaction, which however does not reflect the properties of the studied state.

The negativity [19] is defined as either zero or the absolute value of the smallest negative eigenvalue of a partially transposed density matrix multiplied for convenience by a factor of two

$$N(\rho) = \max[0, -2\min \text{eig}(\rho^\Gamma)], \quad (3)$$

where superscript  $\Gamma$  denotes partial transposition.

The concurrence [18] can be calculated using a formula

$$C(\rho) = \max(0, 2\lambda_{\max} - \sum_j \lambda_j), \quad (4)$$

where  $\lambda_j^2 = \text{eig}[\rho(Y \otimes Y)\rho^*(Y \otimes Y)]$ ,  $\lambda_{\max} = \max_j \lambda_j$ , symbol  $*$  denotes complex conjugation and  $Y$  is the Pauli operator.

The REE [20] is defined as the distance to the closest separable state given by the Kullback-Leibner distance, i.e.

$$\text{REE}(\rho) = \max_{\rho_{\text{sep}} \in \mathcal{D}} S(\rho || \rho_{\text{sep}}), \quad (5)$$

where  $S(\rho || \rho_{\text{sep}}) = \text{Tr}(\rho \log_2 \rho - \rho \log_2 \rho_{\text{sep}})$  and  $\mathcal{D}$  is the set of all two-qubit separable states.

One can define the potentials for negativity (NP), concurrence (CP) and relative entropy of entanglement (REEP) as

$$\text{NP}_{wr}[\sigma(p, y)] = N[\rho_{wr}(p, y)], \quad (6)$$

$$\text{CP}_{wr}[\sigma(p, y)] = C[\rho_{wr}(p, y)], \quad (7)$$

$$\text{REEP}_{wr}[\sigma(p, y)] = \text{REE}[\rho_{wr}(p, y)]. \quad (8)$$

Note that the potential is attributed to the single-mode state  $\sigma$  by evaluating entanglement of the two-mode state  $\rho$ .

## III. EXPERIMENTAL SETUP

We have constructed an experimental setup on the platform of linear optics (see Fig. 2). As mentioned above, we employ the polarization encoding, where the

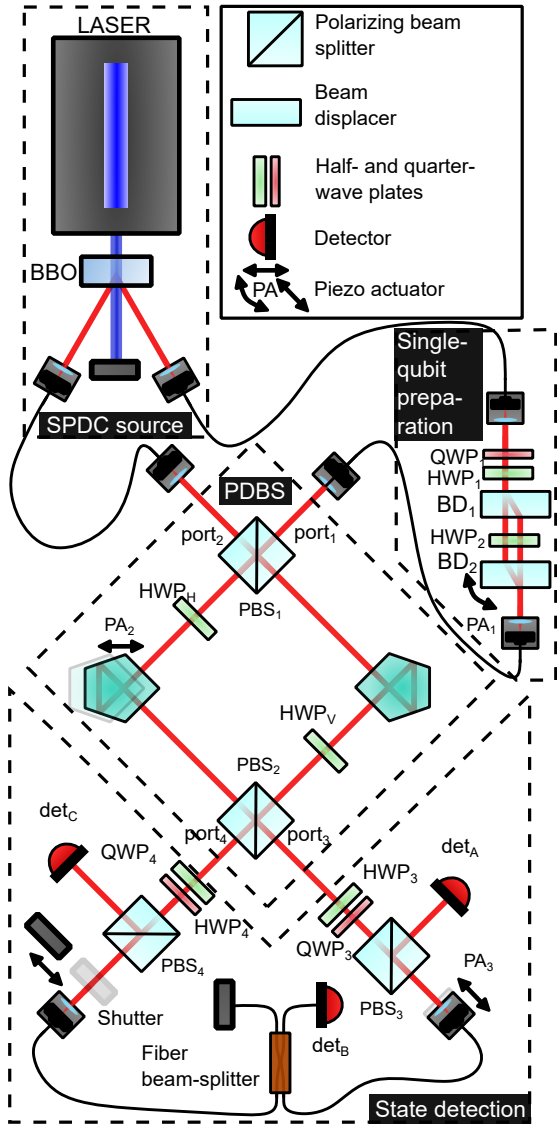


FIG. 2. Scheme of the experimental setup. SPDC stands for spontaneous parametric down-conversion, BBO denotes beta barium borate ( $\beta$ -BaB<sub>2</sub>O<sub>4</sub>) crystal and PDBS means polarization dependent beam splitter.

horizontal component of the polarization represents the single photon state, while the vertically polarized component represents the vacuum state, since the vertically polarized photon has the vacuum in its horizontal-polarization mode.

Separable photon-pairs are generated using a type-I spontaneous parametric down conversion (SPDC). One photon from each pair is guided through an optical fibre into the *single-qubit preparation* stage. There, using a set of motorized quarter- (QWP) and half-wave (HWP) plates, the photon is transformed into any pure single qubit state in the form of Eq. (1) with  $D = 1$ . To tune the value of  $D$ , a set of two beam displacers (BD) with a half-wave plate rotated by 45° in the middle is used.

The second BD can be tilted by a piezo actuator, allowing to set a path difference and, thus, a phase shift ( $\Delta\phi$ ) between the two polarization components. By changing randomly, with probability  $f$ , between the identity ( $\Delta\phi = 0$ ) and the phase flip ( $\Delta\phi = \pi$ ) operations, a desired value of  $D$  is achieved. The single qubit is then guided through another optical fibre into the first port of the *polarization dependent beam splitter* (PDBS). Second photon from each pair is vertically polarized, as it plays the role of pure vacuum, and is guided directly from the SPDC source into the second port of the PDBS.

The PDBS is implemented by means of a Mach-Zehnder interferometer constructed from two polarizing beam splitters (PBS) with a motorized HWP in each arm. The horizontal (vertical) polarization components of both photons meet in the arm<sub>H</sub> (arm<sub>V</sub>) after implementing a bit-flip operation to one of the inputs (HWP<sub>2</sub>). The reflection coefficients for each polarization component are set by the rotation of the waveplates:  $r_{H;V} = \sin 2\theta_{H;V}$ . Rotation of HWP<sub>3</sub> is offset by 45° to compensate for the initial bit-flip operation. For all measurements, the  $\theta_V$  is set to 22.5°, accomplishing a balanced splitting for the vertical polarization component, corresponding to the symmetric behavior of the vacuum on a beam splitter, while  $\theta_H$  is tuned.

Due to the specific nature of the encoding in use, particularly due to the bunching of the vertically polarized photons holding place for the vacuum, we cannot use a standard quantum tomography. We designed a special detection apparatus and procedure to reconstruct the output state density matrix. The detection apparatus consists of a set of wave plates followed by a polarizing beam splitter in both of the output ports of the PDBS. One output port of each of these splitters is guided directly to a single-photon detector, while the other is led to a fibre beam splitter, whose one output is then guided to a third detector. Using coincidence logic, events consisting of simultaneous detections by two detectors are registered.

The reconstructed density matrix takes the form of

$$\rho_{out} = \begin{pmatrix} \rho_{11} & \rho_{12} & \rho_{13} & 0 \\ \rho_{21} & \rho_{22} & \rho_{23} & 0 \\ \rho_{31} & \rho_{32} & \rho_{33} & 0 \\ 0 & 0 & 0 & 0 \end{pmatrix} = \begin{pmatrix} M_A & M_C & M_D & 0 \\ M_C^* & M_B & 0 & 0 \\ M_D^* & 0 & 0 & 0 \\ 0 & 0 & 0 & 0 \end{pmatrix}, \quad (9)$$

where we will assume only the absolute value of the off-diagonal elements, because any state in Eq. (2) can be transformed into a fully positive matrix, using only local rotations and as a result the entanglement measures are independent of the phases in  $\rho_{out}$ .

We split the detection procedure into several steps corresponding to the blocks in the matrix in Eq. (9).

The term  $M_A$  corresponds to the case of two vertically polarized photons on the input. Due to the rotation of HWP<sub>V</sub> and the Hong-Ou-Mandel effect [22], the photons bunch at the output of the PDBS, meaning they are both either in one output port or the other. Due to the fact that they propagate symmetrically in both arms and that

the vertical polarization serves only as a placeholder for the vacuum, we register the signal only in one arm and correct for the undetected signal accordingly. The term is measured using  $\text{det}_A$  and  $\text{det}_B$ , while the shutter in  $\text{port}_4$  is closed and wave plates in  $\text{port}_3$  are set, so that the bunched photons split in half of the cases. Overall, the measured signal is multiplied by the factor of four (two by focusing only on one output arm and another two due to the splitting probability).

The term  $M_B$  corresponds to the case of one horizontal photon in either  $\text{port}_3$  ( $\rho_{22}$ ) or  $\text{port}_4$  ( $\rho_{33}$ ) and the coherence factor between these cases ( $\rho_{23}$ ). The vertically polarized component propagates symmetrically in both output arms. In this case, we register the vertically polarized component in the output port other than that where the horizontal component is detected. To correct for neglecting the vertical component in the other arm, we multiply the signal by the factor of two. The submatrix  $M_B$  itself is measured by a standard two-qubit state tomography [23, 24] using  $\text{det}_A$  and  $\text{det}_C$  and a maximum likelihood estimation is applied. This leads to a matrix in the form

$$\rho_B = \begin{pmatrix} 0 & 0 & 0 & 0 \\ 0 & \tilde{M}_B & 0 & 0 \\ 0 & 0 & 0 & 0 \\ 0 & 0 & 0 & 0 \end{pmatrix}, \quad (10)$$

where  $\tilde{M}_B$  is normalized  $M_B$ . A proper renormalization takes into account the measurement of  $M_A$ .

To acquire the  $M_D$  term, we measure directly the coherence between  $\rho_{11}$  and  $\rho_{33}$  via an interference pattern on the fibre beam splitter using the detectors  $\text{det}_A$  and  $\text{det}_B$ . In  $\text{port}_3$ , we project onto the term  $\rho_{11}$  using the same setting as when measuring  $M_A$ . In  $\text{port}_4$ , the shutter is left open and the waveplates are set such that the term  $\rho_{33}$  is projected onto the same set of detectors, leading to the interference of the two projected terms. A piezo-driven ( $\text{PA}_3$ ) phase shift is used to sweep through the whole interference pattern, whose maximum and minimum can be used to calculate the absolute value of the coherence term. Due to the instability of the interference pattern, it is not possible to determine the phase of  $M_D$ , but as mentioned above, we can focus only on the absolute value of the off-diagonal terms.

Using the same measurement method with settings symmetrically swapped for  $\text{port}_3$  and  $\text{port}_4$ , we acquire the value of  $M_C$ .

For more details about the measurement procedure, see [17], where we used this setup for a conceptually different experiment.

#### IV. EXPERIMENTAL RESULTS

In this work, we analyse three experimentally obtained classes of states: (i) pure input states and coherent interaction with the vacuum (BS parameter  $r \in [0, 1]$ ,  $w = 1$ )

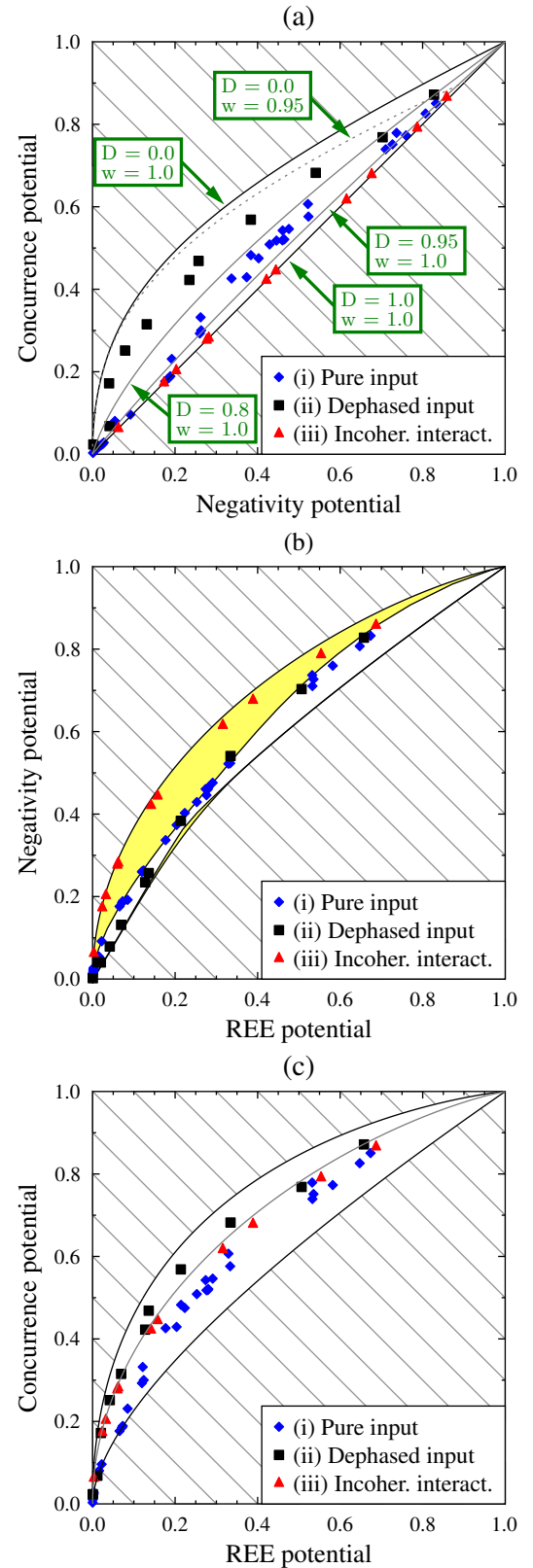


FIG. 3. Mutual relations between the observed potentials for various entanglement measures for the experimental states of all the three classes (i)- (iii). The grey middle line in the plot (c) corresponds to theoretical prediction for class (iii).

	Class of states	$p$	$y$	$r$	$w$
(i)	Pure input	$[0,1]$	$y_{\max}$	$[0,1]$	1
(ii)	Dephased input	$[0,1]$	0	$1/\sqrt{2}$	1
(iii)	Incoherent interaction	1	$0=y_{\max}$	$1/\sqrt{2}$	$[0,1]$

TABLE I. Classes of experimentally measured states, where  $p$  is the single photon probability,  $y$  is the coherence parameter,  $y_{\max} = \sqrt{p(1-p)}$  is the maximum value of the coherence parameter,  $r$  is the reflectivity amplitude and  $w$  characterizes the output state coherence.

(ii) dephased input states and coherent interaction with the vacuum and (iii) one-photon state subjected to an incoherent interaction with the vacuum with varying incoherence parameter. For the ranges of density matrix parameters see Table I.

To verify that the setup is properly adjusted and the produced states qualify as the class (i), we laid down a condition on the value of the off-diagonal terms:  $\sqrt{\rho_{12}/\rho_{12}^{\max}}\sqrt{\rho_{13}/\rho_{13}^{\max}} > 0.5$ , where  $\rho_{1j}^{\max} = \sqrt{\rho_{11}\rho_{jj}}$  is the maximal possible value of  $\rho_{1j}$  given the values of  $\rho_{11}$  and  $\rho_{jj}$  for  $j \in \{2, 3\}$ .

The incoherent interaction needed to prepare states of the class (iii) was achieved by randomly swapping  $\theta_H$  between  $\pm 22.5^\circ$  and summing the registered coincidence counts.

For all of the output states, we calculated the three entanglement measures: the negativity, the concurrence, and the REE. All these quantities were estimated with uncertainties typically below 0.03. In Fig. 3 we plotted their mutual relations for the measured states. In all three plots, the hatched area represents mutual relations unphysical for any two-qubit state. In the Fig. 3(a) we show the mutual relation between the negativity and the concurrence for the experimental states. This relation allows to separate dephased input states from pure input states independently on the (in)coherence of the interaction. For a better understanding, this plot depicts theoretical loci for states of various parameters  $D$  and  $w$ .

In the second plot, Fig. 3(b), there are two physically possible areas. The white inner area represents the region attainable with any input state interacting on a coherent balanced beam splitter. The extended yellow area is only achievable if the interaction is either incoherent (upper larger area) or the beam splitter is unbalanced (small lower area). As a result, by analysing the mutual relation between REE and negativity, we can clearly uncover imperfections in the interaction. See how the states of class (iii) clearly lie within the yellow area while all other states remain in the white region (up to experimental imperfections). Note that the smaller yellow area on the right-hand side is theoretically reachable by unbalanced beam splitting. In experiment, this area proved to be unattainable due to the fact, that the area is very small

and that dephasing of the output (and other experimental imperfections) pushes the states to the left-hand side of the figure. This shortcoming, however, does not diminish the main point shown by this plot. Observing the hierarchy outside of the white area signals imperfection in the interaction and warns that the observed potentials underestimate the true entanglement potentials of the tested state.

The last plot, Fig. 3(c), depicts the relation between concurrence and relative entropy of entanglement. Although this plot does not provide any new insight, it is plotted for complementarity.

All raw and processed experimental data along with the processing scripts are provided as a Digital Supplement [25].

## V. CONCLUSIONS

We have both theoretically and experimentally analyzed hierarchies among three entanglement potentials, i.e. the negativity, concurrence, and REE potentials for three typical classes of states. Our experimental results are consistent with previous theoretical expectations, namely in the sense of mutual hierarchies reachable by states belonging to these classes.

Most importantly, we have documented the benefits of studying the hierarchies as they allow to detect imperfect interaction between the tested state and the classical state. Detecting imperfections in the interaction is critical in preventing misjudging the states' true nonclassicality. Considering that imperfections are unavoidable in experimental reality, especially in near-future quantum technologies, we believe that our findings are relevant for the practical deployment of entanglement potentials as a method for nonclassicality quantification.

Further analysis can be performed allowing to establish markers of various interaction flaws (decoherence, amplitude damping). One can, for instance, immediately deduce the incoherence of the interaction by comparing the absolute value of the term  $\rho_{12}$  to its maximum value  $\rho_{12}^{\max}$ . Our analysis, however, enables to estimate the impact of this incoherence on the observed entanglement potentials.

## ACKNOWLEDGEMENTS

J.K gratefully acknowledges the support from the project IGA\_PrF\_2023\_005 of Palacký University. AČ and KM acknowledge support by the project OP JAC CZ.02.01.01/00/22\_008/0004596 of the Ministry of Education, Youth, and Sports of the Czech Republic. We thank Cesnet for data management services.

- 
- [1] C. H. Bennett and G. Brassard, Quantum cryptography: Public key distribution and coin tossing, *Theor. comp. sci.* **560**, 7 (2014).
  - [2] P. W. Shor and J. Preskill, Simple proof of security of the BB84 quantum key distribution protocol, *Phys. Rev. Lett.* **85**, 441 (2000).
  - [3] A. K. Ekert, Quantum cryptography based on Bell's theorem, *Phys. Rev. Lett.* **67**, 661 (1991).
  - [4] M. A. Nielsen and I. L. Chuang, *Quantum Computation and Quantum Information: 10th Anniversary Edition* (Cambridge: Cambridge University Press, 2010).
  - [5] E. J. S. Fonseca, C. H. Monken, and S. Pádua, Measurement of the de Broglie wavelength of a multiphoton wave packet, *Phys. Rev. Lett.* **82**, 2868 (1999).
  - [6] J. Jacobson, G. Björk, I. Chuang, and Y. Yamamoto, Photonic de broglie waves, *Phys. Rev. Lett.* **74**, 4835 (1995).
  - [7] R. J. Glauber, *Quantum theory of optical coherence: selected papers and lectures* (John Wiley & Sons, 2007).
  - [8] M. Hillery, Nonclassical distance in quantum optics, *Phys. Rev. A* **35**, 725 (1987).
  - [9] C. T. Lee, Measure of the nonclassicality of nonclassical states, *Phys. Rev. A* **44**, R2775 (1991).
  - [10] N. Lütkenhaus and S. M. Barnett, Nonclassical effects in phase space, *Phys. Rev. A* **51**, 3340 (1995).
  - [11] J. K. Asbóth, J. Calsamiglia, and H. Ritsch, Computable measure of nonclassicality for light, *Phys. Rev. Lett.* **94**, 173602 (2005).
  - [12] A. Miranowicz, K. Bartkiewicz, A. Pathak, J. Peřina, Y.-N. Chen, and F. Nori, Statistical mixtures of states can be more quantum than their superpositions: Comparison of nonclassicality measures for single-qubit states, *Phys. Rev. A* **91**, 042309 (2015).
  - [13] A. Kenfack and K. Życzkowski, Negativity of the wigner function as an indicator of non-classicality, *Journal of Optics B: Quantum and Semiclassical Optics* **6**, 396 (2004).
  - [14] A. Mari, K. Kieling, B. M. Nielsen, E. S. Polzik, and J. Eisert, Directly estimating nonclassicality, *Phys. Rev. Lett.* **106**, 010403 (2011).
  - [15] A. Miranowicz, J. Kadlec, Bartkiewicz, A. Černocho, Y.-N. Chen, K. Lemr, and F. Nori, Quantifying nonclassicality of vacuum-one-photon superpositions via potentials of Bell nonlocality, quantum steering, and entanglement, e-print arXiv:2309.12930 (2023).
  - [16] A. Miranowicz, M. Bartkowiak, X. Wang, Y.-x. Liu, and F. Nori, Testing nonclassicality in multimode fields: A unified derivation of classical inequalities, *Phys. Rev. A* **82**, 013824 (2010).
  - [17] J. Kadlec, K. Bartkiewicz, A. Černocho, K. Lemr, and A. Miranowicz, Experimental hierarchy of the nonclassicality of single-qubit states via potentials for entanglement, steering, and bell nonlocality, *Opt. Express* **32**, 2333 (2024).
  - [18] W. K. Wootters, Entanglement of formation of an arbitrary state of two qubits, *Phys. Rev. Lett.* **80**, 2245 (1998).
  - [19] G. Vidal and R. F. Werner, Computable measure of entanglement, *Phys. Rev. A* **65**, 032314 (2002).
  - [20] V. Vedral, M. B. Plenio, M. A. Rippin, and P. L. Knight, Quantifying entanglement, *Phys. Rev. Lett.* **78**, 2275 (1997).
  - [21] A. Miranowicz, K. Bartkiewicz, N. Lambert, Y.-N. Chen, and F. Nori, Increasing relative nonclassicality quantified by standard entanglement potentials by dissipation and unbalanced beam splitting, *Phys. Rev. A* **92**, 062314 (2015).
  - [22] C. K. Hong, Z. Y. Ou, and L. Mandel, Measurement of subpicosecond time intervals between two photons by interference, *Phys. Rev. Lett.* **59**, 2044 (1987).
  - [23] M. Jeřek, J. Fiurářek, and Z. Hradil, Quantum inference of states and processes, *Phys. Rev. A* **68**, 012305 (2003).
  - [24] E. Halenková, A. Černocho, K. Lemr, J. Soubusta, and S. Drusová, Experimental implementation of the multifunctional compact two-photon state analyzer, *Appl. Opt.* **51**, 474 (2012).
  - [25] Digital Supplement containing raw and processed experimental data along with the processing scripts is available on the publisher's website at <https://...>